How to cite: *Angew. Chem. Int. Ed.* **2024**, *63*, e202408894
doi.org/10.1002/anie.202408894

Heterogeneous Catalysis | Hot Paper

Unveiling Highly Sensitive Active Site in Atomically Dispersed Gold Catalysts for Enhanced Ethanol Dehydrogenation

Ji Yang[+], Juan Zheng[+], Chaochao Dun[+], Lorenz J. Falling, Qi Zheng, Jeng-Lung Chen, Miao Zhang, Nicholas R. Jaegers, Chithra Asokan, Jinghua Guo, Miquel Salmeron, David Prendergast, Jeffrey J. Urban, Gabor A. Somorjai,* Yanbing Guo,* and Ji Su**

Abstract: Developing a desirable ethanol dehydrogenation process necessitates a highly efficient and selective catalyst with low cost. Herein, we show that the "complex active site" consisting of atomically dispersed Au atoms with the neighboring oxygen vacancies (Vo) and undercoordinated cation on oxide supports can be prepared and display unique catalytic properties for ethanol dehydrogenation. The "complex active site" Au–Vo–Zr^{3+} on Au_1/ZrO_2 exhibits the highest H_2 production rate, with above 37,964 mol H_2 per mol Au per hour (385 $g H_2 g_{Au}^{-1} h^{-1}$) at 350 °C, which is 3.32, 2.94 and 15.0 times higher than Au_1/CeO_2, Au_1/TiO_2, and Au_1/Al_2O_3, respectively. Combining experimental and theoretical studies, we demonstrate the structural sensitivity of these complex sites by assessing their selectivity and activity in ethanol dehydrogenation. Our study sheds new light on the design and development of cost-effective and highly efficient catalysts for ethanol dehydrogenation. Fundamentally, atomic-level catalyst design by colocalizing catalytically active metal atoms forming a structure-sensitive "complex site", is a crucial way to advance from heterogeneous catalysis to molecular catalysis. Our study advanced the understanding of the structure sensitivity of the active site in atomically dispersed catalysts.

Introduction

Ethanol dehydrogenation is an important industrial process to produce acetaldehyde and ethyl acetate,[1–3] which are high-value-added chemicals with wide applications in chemical synthesis and the solvent industry. The growing production of bio-ethanol from biomass (such as cassava and cellulose) upgrading in recent decades, makes this process more attractive.[4] Besides, ethanol dehydrogenation is a critical step in the ethanol-liquid organic hydrogen carrier (LOHC) cycle system.[5,6] Therefore, it is desirable to develop low-cost, highly efficient, and selective catalysts for ethanol dehydrogenation. Noble metal catalysts usually display higher ethanol conversion activity than commercial copper catalysts, but their high cost limits the wide applications.[7–9] Atomically dispersed catalysts (ADCs)[10,11] can reduce the catalyst cost by downsizing metal nanoparticles to single atoms, achieving the maximum utilization efficiency of expensive metals. ADCs with uniform distribution of active atoms benefit the new catalyst design for achieving high catalytic activity and selectivity.[12–14]

Designing advanced ADCs for a specific reaction necessitates a comprehensive understanding of two distinct types of interactions: 1) the interaction of atomically dispersed metal with the supporting material; 2) the interaction of the active site with reactant and intermediates. Generally, the interactions between dispersed metal atoms and matrix oxides involve similar phenomena of charge transfer and

[*] Dr. J. Yang,[+] Dr. J. Su
Energy Storage and Distributed Resources Division
Lawrence Berkeley National Laboratory
94720 Berkeley, California, United States
E-mail: jisu@lbl.gov

Dr. J. Yang,[+] J. Zheng,[+] Prof. Y. Guo
College of Chemistry,
Central China Normal University
430079 Wuhan, People's Republic of China
E-mail: guoyanbing@mail.ccnu.edu.cn

Dr. J. Yang,[+] Dr. C. Dun,[+] Dr. D. Prendergast, Dr. J. J. Urban
The Molecular Foundry
Lawrence Berkeley National Laboratory
94720 Berkeley, California, United States
E-mail: jjurban@lbl.gov

Dr. L. J. Falling, Dr. J.-H. Guo
Advanced Light Source
Lawrence Berkeley National Laboratory
94720 Berkeley, California, United States

Q. Zheng, Prof. M. Salmeron
Materials Sciences Division
Lawrence Berkeley National Laboratory
94720 Berkeley, California, United States

Dr. J.-L. Chen
National Synchrotron Radiation Research Center
Science-Based Industrial Park
30076 Hsinchu, Taiwan

Dr. M. Zhang, Dr. N. R. Jaegers, Dr. C. Asokan, Prof. G. A. Somorjai
College of Chemistry
University of California-Berkeley
94720 Berkeley, California, United States
E-mail: somorjai@berkeley.edu

[+] These authors contributed equally to this work.

species spillover with supported metal nanoparticle catalysts, named metal-support interaction (MSI),[15,16] where the active sites were thought to be the interface or peripheral atoms of the nanoparticle in contact with the oxide support.[17] The distinction lies in ADCs, where the co-localization of a single metal atom with neighboring support atoms and surface functional groups can form a "complex active site" characterized by a specific and identifiable structure. On reducible oxide supports the single metal atoms have been reported to locate at anion defects (eg. oxygen vacancy), and cation vacancies through atom migration induced by surface reconstruction due to thermodynamic favorability. For example, single metal atoms can be immobilized onto cation vacancies of reducible CeO_2[18–23] or ZrO_2[24–26] supports in the form of single metal atom-oxygen vacancy-undercoordinated cation. The immobilization of single metal atoms on a reducible support such as CeO_2, will create more oxygen vacancies and undercoordinated Ce^{3+}.[18–22] On TiO_2 support, Au atom will occupy the oxygen vacancy (Vo) and form an Au–Ti complex[27–30] due to favorable thermodynamics, which has been confirmed both theoretically and experimentally. For irreducible oxides such as Al_2O_3 as support, single metal atoms will be anchored by terminal surface hydroxyl group (–OH)/lattice oxygen (O^{2-}).[31–33]

Previous studies have reported the structure and advanced catalytic performance of these complex active sites. For example, our recent studies demonstrated that the immobilization of a single Pt atom onto reducible CeO_2 support generates super-synergy effects between the Pt–Vo–Ce^{3+}, which cooperatively facilitate the adsorption, activation, reaction, and desorption of the reactant, intermediates, and products.[18–22] Recent studies also show that the combination of a single metal atom with Vo and surrounding metal ions on supports can enhance the reaction rate and control the desired product selectivity.[34,35] However, a systematic study of these complex active sites, especially, in interacting with reactants and intermediates remains unaddressed. And manipulating the structure of active complex sites for achieving desired catalytic performance has not been studied. Therefore, exploring the multiple interactions of these complex active sites is highly desirable for advancing catalyst development in ethanol dehydrogenation and furthering the progress in the field of ADCs.

In this work, we prepared four representative ADC samples by loading single Au atoms on ZrO_2, CeO_2, TiO_2, and Al_2O_3 supports. We investigated the performance of different Au-complex site created in these ADCs for ethanol dehydrogenation. *In-situ* diffuse reflectance infrared transform spectroscopy (DRIFTS), ambient pressure X-ray photoelectron spectroscopy (APXPS), and density functional theory (DFT) calculations were employed to understand the structure sensitivity of Au-complex site for ethanol dehydrogenation.

Results and Discussion

The Formation of Au-Complex Sites

Firstly, we used low Au loading (≤ 0.04 wt % determined by inductively coupled plasma optical emission spectroscopy) to ensure all Au atoms are isolated as single atoms (Table S1) and no Au nanoclusters formation was detected by aberration-corrected high-angle annular dark-field scanning transmission electron microscopy (AC-HAADF-STEM) images (Figure 1a–1d and Figure S1). No Au nanocluster formation was detected by further AC-HAADF-STEM examinations (Figure S2). The X-ray diffraction (XRD) detections (Figure S3) further confirmed that there were no additional diffraction lines attributed to the aggregated Au nanoparticles. X-ray absorption near-edge structure (XANES) spectra (Figure S4) detected various ionic $Au^{\delta+}$ ($0<\delta\leq 1$), indicating the coordination state of these atomically dispersed Au atoms are different.

Secondly, X-ray photoelectron spectroscopy (XPS) and electron paramagnetic resonance (EPR) were used to study the single metal atom-support interaction and the surface chemical states of these as-synthesized ADCs. **1)** For the reducible supports of ZrO_2 and CeO_2, Au atoms anchoring onto cation vacancy results in an increase in the amount of unsaturated coordinated cations (Zr^{3+}/Ce^{3+}) and oxygen vacancies in Au_1/ZrO_2 and Au_1/CeO_2 (Figure S5–S6 and Table S2). Furthermore, the increased intensity of EPR signals corresponding to Zr^{3+} ($g=1.996$)[36–39] and Ce^{3+} ($g=1.97$ and 1.94)[40,41] and single electron trapped-oxygen vacancy (Vo·, $g=2.05/2.02$)[41–44] further confirmed the immobilization process above. In addition, the smaller linewidth of the characteristic EPR signal for Zr^{3+} ($g=1.996$, Au_1/ZrO_2) and Ce^{3+} (1.97, Au_1/CeO_2) compared to their blank supports substantiates the transition of electronic microenvironment/electron coupling state, implying electronic structure modulation of ADCs by Au atom immobilization.[45] **2)** For the second type of reducible support of TiO_2, it is notable that Au site insertion decreased the concentration of surface Ti^{3+} and Vo (Figure S7 and Table S2), implied by the decreased deconvoluted area (Vo and Ti^{3+}) of XPS and EPR characteristic signals (Ti^{3+}, $g=1.94$ and Vo·, $g=2.008$).[46–48] This is resulted from the immobilization of Au atom onto the location of oxygen vacancy site.[27–29,49] **3)** For the irreducible support of Al_2O_3, the Au adsorption has no noticeable effects on the chemical state of Al_2O_3 surface, with the evidence of similar binding energy of Al 2p and relatively isotropy electron density around oxygen atoms (Figure S8a and S8b),[50,51] as well as the absence of characteristic signal ($g=2.001$) assigned to Vo· (Figure S8c). Therefore, it is concluded that Au single sites are bonded by surface oxygen of Al_2O_3.[31–33] Scheme S1 summarized the variations of Au complex sites: embedded Au surrounded by oxygen vacancies (ZrO_2 and CeO_2 as supports); anchored Au on oxygen vacancy (TiO_2 as support) and stabilized Au bonding to surface oxygen (Al_2O_3 as support). The nature of oxide supports and the thermodynamics of Au-support interaction during the cata-

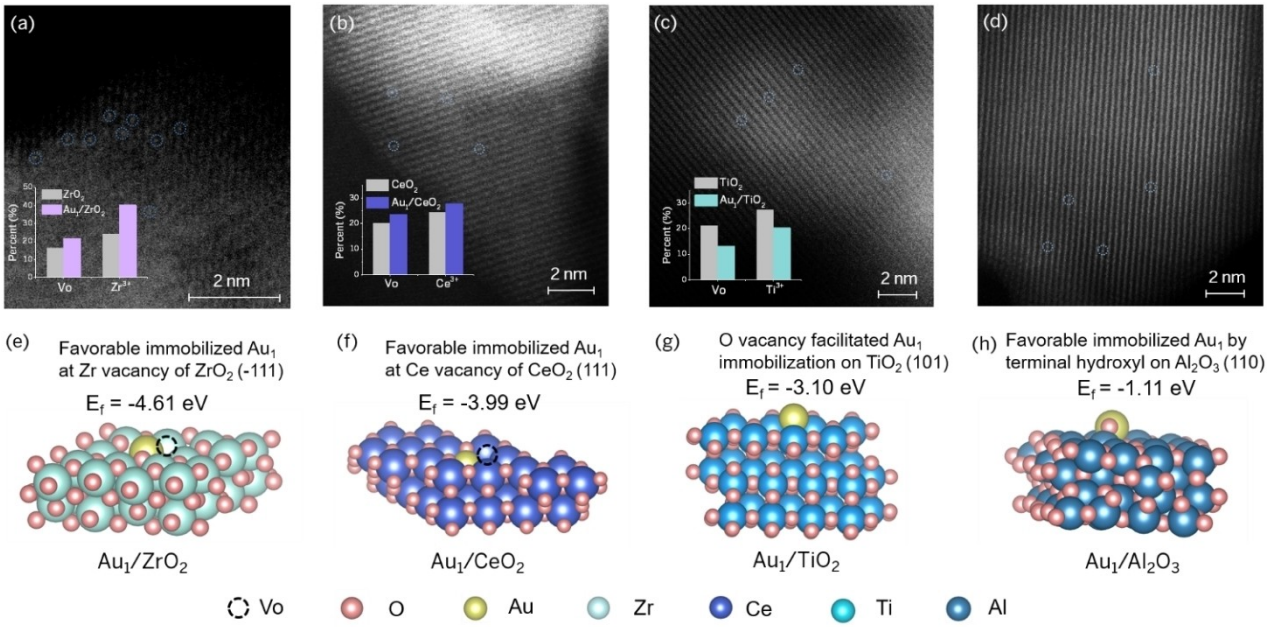

Figure 1. The optimized structure of four ADC prototypes. AC-HAADF-STEM images for (a) Au_1/ZrO_2, (b) Au_1/CeO_2, (c) Au_1/TiO_2, and (d) Au_1/Al_2O_3. Atomically dispersed Au atoms are highlighted by blue circles. The insets in Figure 1a–1c show the percent evolution of oxygen vacancy (Vo) and coordinatively unsaturated metal ions (Zr^{3+}, Ce^{3+}, Ti^{3+}) for the catalysts before and after Au atom insertion based on XPS deconvolution (Figure S5–S7); DFT models of Au atom on various oxide supports: (e) Zr vacancy immobilized Au_1 on ZrO_2 (−111), (f) Ce vacancy immobilized Au_1 on CeO_2 (111), (g) Vo immobilized Au_1 on TiO_2 (101), and (h) Terminal hydroxyl stabilized Au_1 on Al_2O_3 (110).

lyst fabrication process are the major drivers for the formation of Au complex sites with diverse geometries.

Thirdly, DFT calculations were employed to demonstrate the structure of Au complex sites (Figure 1e–1h, Figure S9). DFT modeling results in Figure 1e, 1f, and Figure S9a, S9b show that Au atom immobilized at Zr or Ce vacancy (adjacent to Vo) on ZrO_2 (−4.61 eV) or CeO_2 (−3.99 eV) is more thermodynamically favorable than those at oxygen vacancy (Vo) site (−3.81 eV and −2.99 eV, respectively). For TiO_2 support (Figure 1g and Figure S9c), Au atom anchoring at Vo (−3.10 eV) is more favorably energetic than other location (−1.48 eV). Moreover, Vo facilitates the formation of Au–Ti complex, with a much lower formation energy (−3.10 eV) than perfect TiO_2 (−0.42 eV, −0.37, and −0.13 eV, respectively) (see details in the Supporting Information). The Au atom at Al_2O_3 is more favorably anchored by the terminal hydroxyl group (−1.11 eV) rather than lattice oxygen adsorption (−0.85 eV) (Figure 1h and Figure S9d).

Au-Complex Sites in Ethanol Dehydrogenation

After identifying the Au-complex sites of these ADC Au catalysts, we further explored their effects on ethanol dehydrogenation. At 275 °C, Au_1/ZrO_2 displayed a TOF of ~11948 h^{-1} for H_2 release, which is 4.01-fold, 3.37-fold, and 32.0-fold higher than those of Au_1/CeO_2 (~2983 h^{-1}), Au_1/TiO_2 (~3544 h^{-1}), and Au_1/Al_2O_3 (373 h^{-1}), respectively (Figure 2a). We also studied the liquid product distributions of these Au ADCs (Figure 2b). The major products of Au_1/ZrO_2 and Au_1/CeO_2 catalysts are acetaldehyde and ethyl acetate. For Au_1/CeO_2 catalyst, certain C_6 products (3-hydroxyal-1-hexaldehyde) were also detected. Notably, the dominant product of Au_1/TiO_2 catalyst is acetaldehyde and the major product of Au_1/Al_2O_3 is diethyl ether. The critical role of Au site in catalysis is also confirmed by catalytic results on blank oxide supports (Figure S10), in which Au atom immobilization fundamentally changed the activity and selectivity of ethanol dehydrogenation except Al_2O_3. We also found that a higher reaction temperature favors the ethanol conversion and H_2 generation (Figure S11a). Further increasing the reaction temperature to 350 °C, the TOF of H_2 release for Au_1/ZrO_2 reaches 37,964 h^{-1}, 3.32, 2.94 and 15.0 times higher than Au_1/CeO_2 (11,434 h^{-1}), Au_1/TiO_2 (12,912 h^{-1}), and Au_1/Al_2O_3 (2,531 h^{-1}), respectively (Figure S11a). We noticed that higher temperature triggers the generation of complex liquid products such as C_4 (crotyl alcohol) and C_6 (hexaldehyde, heptanone) products which significantly decreases the selectivity of acetaldehyde (Figure S11b, Table S4 and Scheme S2). For the gas products, a trace amount of ethylene (originated from intramolecular dehydration of ethanol) was detected above 350 °C with no detectable CH_4 or CO, indicating no C–C bond cleavage and decarbonylation.[52] We further studied the stability of the Au_1/ZrO_2 catalyst (Figure S11c). As expected, the catalyst displayed a higher stability under reaction temperature of 275 °C with a relatively lower H_2 productivity than those at higher reaction temperatures (300 and 350 °C). Moreover, ethanol conversion of >85 % and stability over 12 h has been achieved at ethanol's weight hourly space velocity (WHSV) of 0.75 h^{-1} (275 °C), with acetaldehyde and

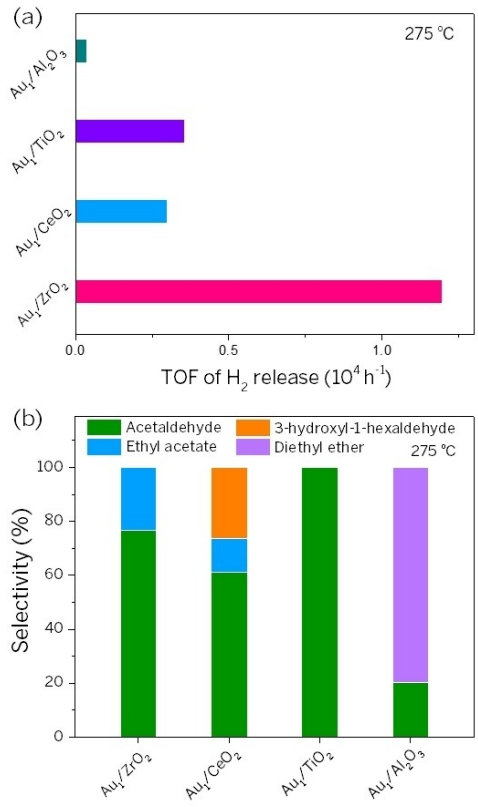

Figure 2. Au-complex site-sensitive ethanol dehydrogenation. (a) Turnover frequency (TOF) of hydrogen production, and (b) liquid product distribution during ethanol dehydrogenation at 275 °C over Au_1/ZrO_2, Au_1/CeO_2, Au_1/TiO_2, and Au_1/Al_2O_3 ADCs with the reaction time of 2 h.

ethyl acetate as major products reaching ~100 % selectivity (Figure S12).

Correlating the Au-complex site with catalytic performance of all Au ADCs, we conclude that: 1) loading single Au atoms on supports of ZrO_2 and CeO_2 creates Au–Vo–undercoordinated ion (Zr^{3+} or Ce^{3+}) complex site after the Au atom immobilization. These complexes work as ensemble reaction pool and display a similar reaction pathway of dehydrogenation and sequent esterification, as well as further aldol condensation under higher temperatures to produce C_4 and C_6 products (Table S4 and Scheme S2); 2) loading single Au atoms on TiO_2 creates Au–Ti complex site due to the Au atom selectively anchoring on the oxygen vacancy, and selectively produce acetaldehyde through ethanol dehydrogenation; 3) loading single Au atoms onto the irreducible support of Al_2O_3 by stabilizing Au atoms with terminal hydroxyl group does not create an obvious synergy between Au and the support, therefore it displays much lower dehydrogenation activity, and the product of diethyl ether was produced by Al_2O_3 support (Figure S10).[53,54]

Synergistic Effect of Au–Vo–Zr^{3+} Complex Site

To further elucidate the Au-complex site-effect of Au ADCs in ethanol dehydrogenation, we used Au_1/ZrO_2 ADC as the primary prototype catalyst, combining with *in-situ* diffuse reflectance infrared Fourier transform spectra (DRIFTS), ambient pressure (AP)-XPS and EPR to study the reaction pathway.

Figures 3a and 3b show the *in-situ* DRIFTS of Au_1/ZrO_2 and ZrO_2 samples with purging ethanol vapor in N_2 under 250 °C. After ethanol adsorption, the C–H stretching vibration bands (~2800–3000 cm^{-1}) and C–O stretching vibration bands (~1000–1200 cm^{-1}) are detected (See detailed bands assignments in Table S6). Especially, C–O stretching vibration can be used to identify the structure of adsorbed ethanol and adsorbed ethoxy species: for blank ZrO_2 sample, the bands at 1150, 1071 and 1050 cm^{-1} in Figure 3a are attributed to molecularly adsorbed ethanol and linearly adsorbed ethoxy species (type *a* or *b*), bridged adsorbed ethoxy species (type *c*) and bridged ethoxy adsorbed on oxygen vacancy (type *d*), respectively (Scheme S3).[55–63] For Au_1/ZrO_2, the enhanced adsorption band at 1050 cm^{-1} (type *d* species) with a relatively decreased adsorption of the other types (1150 and 1071 cm^{-1}) is detected, which indicates Au atoms loading favored the formation of type *d* ethoxy species on the Zr^{3+} in the Au–Vo–Zr^{3+} complex. The ethanol adsorption on Au_1/ZrO_2 is also probed by EPR (Figure S14). The decreased intensity of EPR characteristic signal associated with Vo is detected, which further validates the FTIR analysis that ethoxy is favorable to bind on Zr^{3+} ions surrounding Au–Vo sites. Furthermore, a slight red-shift of C–H stretching vibration at 2962 and 2920 cm^{-1} is found, which indicates ethoxy adsorption at undercoordinated Zr^{3+} due to Au atom insertion.[64,65] More interestingly, visible bands at 1758 and 1720 cm^{-1} assigned to ν(C=O) mode of acetaldehyde (Figure 3a) in the gas phase and a preferential η^1(O)-configuration adsorption[57,60,66] was observed.[52,67,68] We further studied the desorption dynamics of the acetaldehyde and other intermediates species (Figure 3b and Figure S15). After purging with pure N_2 (without ethanol vapor), the type *c* and *d* ethoxy species (1071 and 1050 cm^{-1}) and acetaldehyde species (1758 and 1720 cm^{-1}) are significantly decayed in 2 minutes; While the decay of molecularly adsorbed ethanol and linearly adsorbed ethoxy species (1150 cm^{-1}) is much slower than bridged adsorbed ethoxy species. This indicates that bridged ethoxy species generated at Au–Vo–Zr^{3+} complex are more active than others. The adsorbed crotonaldehyde species (1648 and 1602 cm^{-1}) and acetate species (1559 to 1382 cm^{-1}) are also detected, which have a much slower desorption rate. Correlated with sluggish dynamic features of ethoxy activation/reaction on blank ZrO_2 support (Figure S15), *in-situ* DRIFTS evidenced Au atom insertion enabled much higher C–H bond cleavage efficiency and more favorable acetaldehyde desorption properties.

After resolving surface species evolution from *in-situ* DRIFTS, we conducted *in-situ* AP-XPS study to further monitor the chemical state evolution of the catalyst surface

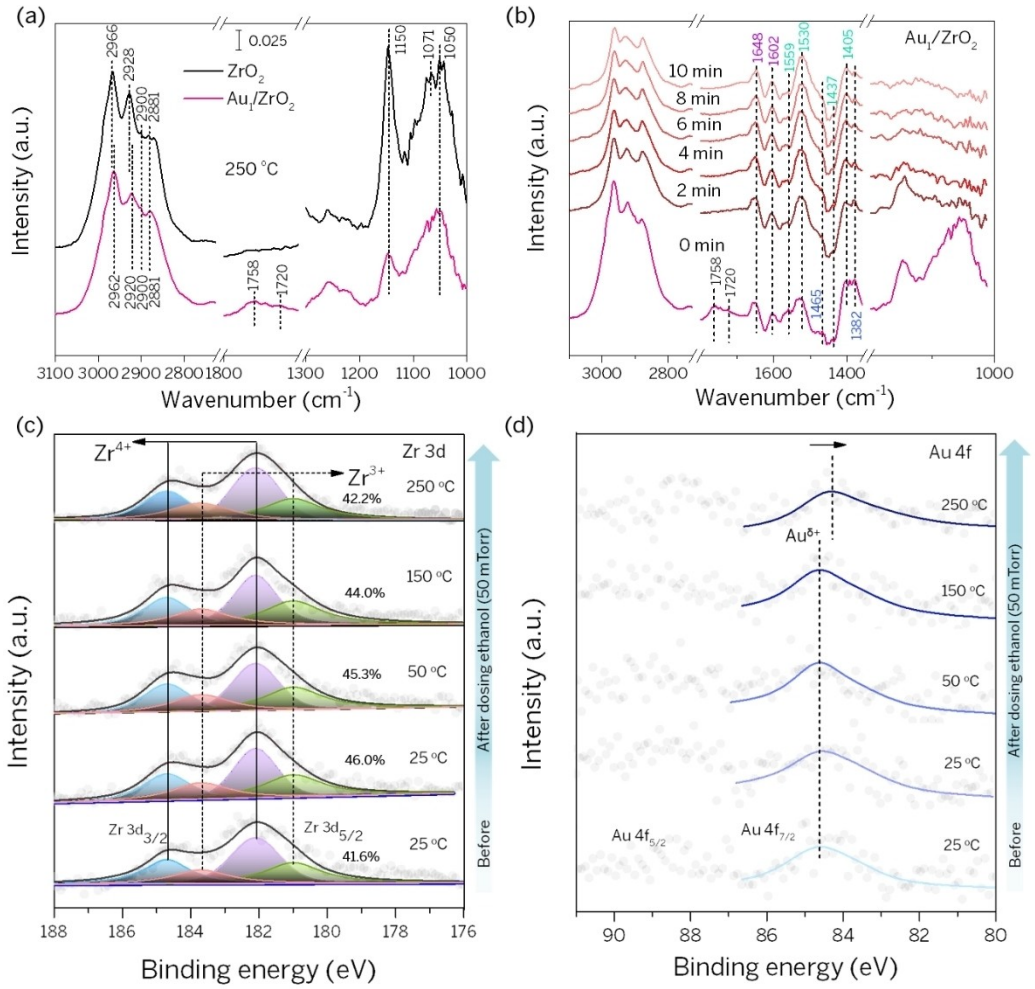

Figure 3. Spectroscopic studies on ethanol dehydrogenation over Au_1/ZrO_2. (a) *In-situ* diffuse reflectance infrared Fourier transform spectra (DRIFTS) of Au_1/ZrO_2 and ZrO_2 when purging with ethanol vapor (with N_2 as carrier gas) at 250 °C; (b) Time-resolved *in-situ* DRIFTS of Au_1/ZrO_2 purged with pure N_2 (without ethanol vapor dosing); *In-situ* AP-XPS (c) Zr 3d and (d) Au 4f spectra for Au_1/ZrO_2 before and after ethanol dosing.

during the reaction (Figure 3c and 3d). The ethanol dosing at low temperatures (25–50 °C) increased the amount of Zr^{3+} species due to the ethoxy species with strong electron-donating capability adsorb on Zr^{4+} site and reduce it to Zr^{3+}. A slight decrease in the amount of Zr^{3+} species from 25 to 50 °C is likely resulting from the ethoxy species desorption.[69,70] Interestingly, the ethanol vapor dosing has no obvious influence on the amount of Au species ($Au^{\delta+}$, $0<\delta<+1$), indicating that the Au site did not participate in the adsorption and activation (deprotonation) of ethanol to ethoxy species. The dehydrogenation of ethoxy species involving the α–C–H bond cleavage through H abstraction by Au atom (validated by DFT calculations in Figure 4 below) occurs at 150 °C and displays decent activity under 250 °C (Figure S11a). Meanwhile, a more obvious decrease in the amount of Zr^{3+} species for Au_1/ZrO_2 was detected at 150 and 250 °C (Figure 3c), due to the transformation of ethoxy species to acetaldehyde species with weakened electron-donating effects. The Au 4*f* binding energy of $Au^{\delta+}$ species shows a slight decrease from 150 to 250 °C, resulting from the reduction effect of H species and electron-donating effect of acetaldehyde species. The above analysis shows that the synergistic effect of the Au–Vo–Zr^{3+} complex site is crucial for ethanol adsorption, activation, reaction, and desorption.

Proposed Ethanol Dehydrogenation Mechanism

We further proposed a reaction mechanism for ethanol dehydrogenation over Au_1/ZrO_2 catalyst (Figure 4, Figure S16–S18). Figure 4a shows that the catalytic cycle is initiated with the ethanol dissociation adsorption at adjacent Zr^{3+}–Vo–Zr^{3+} sites to form bridged-ethoxy-species and Zr–OH ([1]→[2]), then the scission of α–C–H bond (0.45 eV) through H abstraction by Au atom to Au–H hydride ([2]→[3]), followed by H_2 recombination (1.20 eV) and desorption ([3]→[4]), and finally acetaldehyde desorption (0.30 eV) ([4]→[1]). The catalytic cycle of ethanol dehydrogenation to acetaldehyde on Au_1/ZrO_2 is easily closed by this low-energy route. In the next stage, acetaldehyde intermediates would be further attacked by

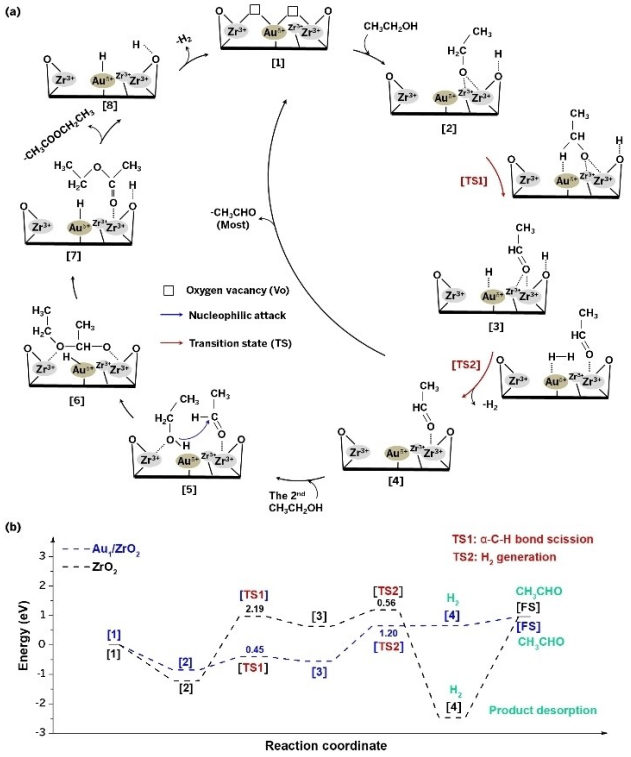

Figure 4. Zr^{3+}–Vo–$Au^{\delta+}$ complex site-mediated ethanol dehydrogenation on Au_1/ZrO_2. (a) Catalytic cycle simulations of ethanol dehydrogenation on Au_1/ZrO_2. (b) The calculated energy profiles of ethanol dehydrogenation to acetaldehyde on Au_1/ZrO_2 and ZrO_2.

newly adsorbed ethanol species at Zr^{3+} ([4]→[5]) to generate ethoxy hemiacetal bridged adsorbed at two Zr atoms ([5]→[6]), followed by the decomposition of ethoxy hemiacetal to ethyl acetate (EA) intermediates at Zr site (0.12 eV) and adjacent Zr–OH ([6]→[7]). Finally, after EA desorption (0.66 eV) and H_2 formation/release ([7]→[8]), the catalytic cycle of ethanol dehydrogenation to EA is accomplished. The energy of EA desorption (0.66 eV) is 0.36 eV higher than acetaldehyde desorption (0.30 eV), indicating the thermodynamic unfavourability of the reaction pathway to generate EA. This explains why acetaldehyde is the major product (with selectivity of $>75\,\%$) from ethanol dehydrogenation on Au_1/ZrO_2 observed in Figure 2b.

We compared the ethanol activation over ZrO_2 and $Au_1/ZrOr_2$ using DFT simulation. The simulated catalytic cycle of ethanol dehydrogenation on ZrO_2 is shown in Figure S17, and the calculated energy profiles are presented in Figure 4b and Figure S18. The rate-determining step (RDS) for ethanol activation on ZrO_2 is the cleavage of the α–C–H bond (2.19 eV) [TS1]. With Au–Vo–Zr^{3+} complex site, the RDS is H_2 formation with an energy barrier of 1.20 eV, which is 0.99 eV lower than that of RDS on ZrO_2 (Table S7). Moreover, Au_1/ZrO_2 exhibited lower reaction energy for acetaldehyde formation (0.29 eV vs. 1.85 eV) ([2]→[3]), acetaldehyde desorption (0.30 eV vs. 3.39 eV) ([4]→[1]) and EA formation (0.12 eV vs. 2.55 eV) ([6]→[7]) than ZrO_2 (Table S8). Therefore, the excellent catalytic activity of Au_1/ZrO_2 catalyst are attributed to the synergistic effects among complex site Au–Vo–Zr^{3+}, which facilitates the elementary steps kinetically and thermodynamically, in the catalytic cycle of ethanol dehydrogenation.

We further studied structure-function relationships of formed Au complex sites by DFT calculations (Figure S19–S23, Table S9–S10). Our results show that Au_1/ZrO_2 and Au_1/CeO_2 have similar Au complex sites (Au–Vo–Zr^{3+} vs. Au–Vo–Ce^{3+}) and display a similar reaction pathway for ethanol dehydrogenation (Figure 4a, S20–S21). Both Au_1/ZrO_2 (−0.85 eV) and Au_1/CeO_2 (−0.72 eV) exhibited favorable ethanol dissociation adsorption to form active ethoxy. The RDS for ethanol activation on both Au_1/ZrO_2 and Au_1/CeO_2 is H_2 formation, rather than α–C–H bond scission (Table S9). The energy barrier of H_2 formation on Au_1/ZrO_2 (1.20 eV) is 0.29 eV lower than that on Au_1/CeO_2 (1.49 eV), which results in a higher H_2 productivity on Au_1/ZrO_2. Comparatively, DFT analysis (Figure S20 and S22) show that the RDS on Au_1/TiO_2, with Au–Ti complex sites, is the cleavage of the α–C–H bond (1.35 eV). We noticed that the energy barrier for the RDS on Au_1/TiO_2 is lower than that on Au_1/CeO_2 (1.35 vs. 1.49 eV). However, ethanol dissociation adsorption to active ethoxy species on Au_1/TiO_2 necessitates a reaction energy of 0.25 eV (Figure S23). By contrast, this adsorption-deprotonation process is thermodynamically favorable on Au_1/CeO_2 (−0.72 eV). Moreover, Au_1/TiO_2 exhibited a higher energy for acetaldehyde desorption than that on Au_1/CeO_2 (0.63 vs. 0.3 eV) (Table S10). The interplay between kinetic and thermodynamic factors thus accounted for a slightly higher H_2 productivity of Au_1/TiO_2 than Au_1/CeO_2.

Conclusion

In summary, we prepared four atomically dispersed Au catalysts using ZrO_2, CeO_2, TiO_2, and Al_2O_3 as supports and evaluated their performances in ethanol dehydrogenation. Combined with systematic spectroscopic studies (XPS, AP-XPS, EPR, *in-situ* DRIFTS) and DFT simulation, we identified the structure of Au complex sites, discussed the structure–activity relationship and proposed reaction mechanism of ethanol dehydrogenation. Specifically, Au_1/ZrO_2 catalyst displays 100 % selectivity of acetaldehyde and ethyl acetate production, and exhibits the most superior activity for ethanol dehydrogenation in terms of H_2 release. The synergy in $Au^{\delta+}$–Vo–Zr^{3+} complex site facilitates ethanol dissociation adsorption at Zr^{3+}, ethoxy activation, and product desorption over $Au^{\delta+}$. The Au_1/CeO_2 catalyst containing $Au^{\delta+}$–Vo–Ce^{3+} complex site displays a similar reaction pathway to Au_1/ZrO_2 catalyst. The Au_1/TiO_2 catalyst creates Au–Ti complex site and favors the acetaldehyde production with 100 % selectivity. The Au_1/Al_2O_3 catalyst displays the lowest H_2 generation rate and the highest diethyl ether selectivity. This work highlights the advantages of ADC design by composing single metal atom with surrounding atoms and functional groups on the support into a complex site, advancing catalyst development

for ethanol dehydrogenation and deepening the understanding of the structure sensitivity of the active site in ADCs.

Author Contributions

J. S., Y. G., J. J. U., and G. A. S. designed research; J. Y., J. Z., and C. D. performed research; J. Y., J. Z., C. D., L. J. F., Q. Z., J. C., M. Z., N. J., C. A., J.-H. G., M. S., and D. P. analyzed data; and J. Y., J. Z., and C. D., G. A. S., J. J. U., Y. G., and J. S. wrote the paper.

Acknowledgments

This work was financially supported by the Hydrogen Materials Advanced Research Consortium (HyMARC), established as part of the Energy Materials Network by the U.S. Department of Energy, Office of Energy Efficiency and Renewable Energy, Fuel Cell Technologies Office, under Contract Number DE-AC02-05CH11231. Spectroscopic and microscopic experiments were performed at the Advanced Light Source (ALS) and Molecular Foundry at LBNL under contract no. DE-AC02-05CH11231. Ji Yang acknowledges the China Scholarship Council for providing his exchange scholarship. Prof. Yanbing Guo acknowledges the support by the National Natural Science Foundation of China (22076060) and the Natural Science Foundation for Distinguished Young Scholars of Hubei Province (2021CFA085).

Conflict of Interest

The authors declare no conflict of interest.

Data Availability Statement

The data that support the findings of this study are available from the corresponding author upon reasonable request.

Keywords: Gold · Site synergy · Atomically-dispersed catalysis · Ethanol dehydrogenation

[1] B. Jørgensen, S. Egholm Christiansen, M. L. Dahl Thomsen, C. H. Christensen, *J. Catal.* **2007**, *251*, 332–337.
[2] J. Pang, M. Zheng, C. Wang, X. Yang, H. Liu, X. Liu, J. Sun, Y. Wang, T. Zhang, *ACS Catal.* **2020**, *10*, 13624–13629.
[3] J. C. Serrano-Ruiz, R. Luque, A. Sepúlveda-Escribano, *Chem. Soc. Rev.* **2011**, *40*, 5266–5281.
[4] C. Manochio, B. R. Andrade, R. P. Rodriguez, B. S. Moraes, *Renewable Sustainable Energy Rev.* **2017**, *80*, 743–755.
[5] C. Mevawala, K. Brooks, M. E. Bowden, H. M. Breunig, B. L. Tran, O. Y. Gutiérrez, T. Autrey, K. Müller, *Energy Technol.* **2023**, *11*, 1–8.
[6] B. L. Tran, S. I. Johnson, K. P. Brooks, S. T. Autrey, *ACS Sustainable Chem. Eng.* **2021**, *9*, 7130–7138.
[7] M. Ouyang, S. Cao, S. Yang, M. Li, M. Flytzani-Stephanopoulos, *Ind. Eng. Chem. Res.* **2020**, *59*, 2648–2656.
[8] Y. Huang, B. Wang, H. Yuan, Y. Sun, D. Yang, X. Cui, F. Shi, *Catal. Sci. Technol.* **2021**, *11*, 1652–1664.
[9] J. Pang, M. Yin, P. Wu, X. Li, H. Li, M. Zheng, T. Zhang, *Green Chem.* **2021**, *23*, 7902–7916.
[10] S. Ji, Y. Chen, X. Wang, Z. Zhang, D. Wang, Y. Li, *Chem. Rev.* **2020**, *120*, 11900–11955.
[11] R. Qin, K. Liu, Q. Wu, N. Zheng, *Chem. Rev.* **2020**, *120*, 11810–11899.
[12] J. Jones, H. Xiong, A. T. DeLaRiva, E. J. Peterson, H. Pham, S. R. Challa, G. Qi, S. Oh, M. H. Wiebenga, X. I. P. Hernández, Y. Wang, A. K. Datye, *Science* **2016**, *353*, 150–154.
[13] J. Shan, M. Li, L. F. Allard, S. Lee, M. Flytzani-Stephanopoulos, *Nature* **2017**, *551*, 605–608.
[14] P. Liu, Y. Zhao, R. Qin, S. Mo, G. Chen, L. Gu, D. M. Chevrier, P. Zhang, Q. Guo, D. Zang, B. Wu, G. Fu, N. Zheng, *Science* **2016**, *352*, 797–801.
[15] Y. Li, Y. Zhang, K. Qian, W. Huang, *ACS Catal.* **2022**, *12*, 1268–1287.
[16] T. W. Van Deelen, C. Hernández Mejía, K. P. De Jong, *Nat. Catal.* **2019**, *2*, 955–970.
[17] Y. Li, M. Kottwitz, J. L. Vincent, M. J. Enright, Z. Liu, L. Zhang, J. Huang, S. D. Senanayake, W. C. D. Yang, P. A. Crozier, R. G. Nuzzo, A. I. Frenkel, *Nat. Commun.* **2021**, *12*, 914.
[18] L. N. Chen, K. P. Hou, Y. S. Liu, Z. Y. Qi, Q. Zheng, Y. H. Lu, J. Y. Chen, J. L. Chen, C. W. Pao, S. B. Wang, Y. Bin Li, S. H. Xie, F. D. Liu, D. Prendergast, L. E. Klebanoff, V. Stavila, M. D. Allendorf, J. Guo, L. S. Zheng, J. Su, G. A. Somorjai, *J. Am. Chem. Soc.* **2019**, *141*, 17995–17999.
[19] Z. Qi, L. Chen, S. Zhang, J. Su, G. A. Somorjai, *J. Am. Chem. Soc.* **2021**, *143*, 60–64.
[20] S. Zhang, L. Chen, Z. Qi, L. Zhuo, J. L. Chen, C. W. Pao, J. Su, G. A. Somorjai, *J. Am. Chem. Soc.* **2020**, *142*, 16533–16537.
[21] L. Chen, Z. Qi, X. Peng, J. L. Chen, C. W. Pao, X. Zhang, C. Dun, M. Young, D. Prendergast, J. J. Urban, J. Guo, G. A. Somorjai, J. Su, *J. Am. Chem. Soc.* **2021**, *143*, 12074–12081.
[22] L. Chen, P. Verma, K. Hou, Z. Qi, S. Zhang, Y. Liu, J. Guo, V. Stavila, M. D. Allendorf, L. Zheng, M. Salmeron, D. Prendergast, G. A. Somorjai, J. Su, *Nat. Commun.* **2022**, *13*, 1092.
[23] B. Qiao, J. Liu, Y. G. Wang, Q. Lin, X. Liu, A. Wang, J. Li, T. Zhang, J. Liu, *ACS Catal.* **2015**, *5*, 6249–6254.
[24] Z. P. Liu, C. M. Wang, K. N. Fan, *Angew. Chem. Int. Ed.* **2006**, *45*, 6865–6868.
[25] K. Harrath, X. Yu, H. Xiao, J. Li, *ACS Catal.* **2019**, *9*, 8903–8909.
[26] Y. Kwon, T. Y. Kim, G. Kwon, J. Yi, H. Lee, *J. Am. Chem. Soc.* **2017**, *139*, 17694–17699.
[27] Z. Hu, C. Yang, K. Lv, X. Li, Q. Li, J. Fan, *Chem. Commun.* **2020**, *56*, 1745.
[28] S. Dong, B. Li, X. Cui, S. Tan, B. Wang, *J. Phys. Chem. Lett.* **2019**, *10*, 4683–4691.
[29] A. Mellor, D. Humphrey, C. M. Yim, C. L. Pang, H. Idriss, G. Thornton, *J. Phys. Chem. C* **2017**, *121*, 24721–24725.
[30] J. Wan, W. Chen, C. Jia, L. Zheng, J. Dong, X. Zheng, Y. Wang, W. Yan, C. Chen, Q. Peng, D. Wang, Y. Li, *Adv. Mater.* **2018**, *30*, 1705369.
[31] T. K. Ghosh, N. N. Nair, *ChemCatChem* **2013**, *5*, 1811–1821.
[32] M. Moses-Debusk, M. Yoon, L. F. Allard, D. R. Mullins, Z. Wu, X. Yang, G. Veith, G. M. Stocks, C. K. Narula, *J. Am. Chem. Soc.* **2013**, *135*, 12634–12645.
[33] F. Wang, J. Ma, S. Xin, Q. Wang, J. Xu, C. Zhang, H. He, X. Cheng Zeng, *Nat. Commun.* **2020**, *11*, 1–9.
[34] S. Xie, L. Liu, Y. Lu, C. Wang, S. Cao, W. Diao, J. Deng, W. Tan, L. Ma, S. N. Ehrlich, Y. Li, Y. Zhang, K. Ye, H. Xin, M.

Flytzani-stephanopoulos, F. Liu, *J. Am. Chem. Soc.* **2022**, DOI 10.1021/jacs.2c08902.
[35] K. Zhang, Q. Meng, H. Wu, J. Yan, X. Mei, P. An, L. Zheng, J. Zhang, M. He, B. Han, *J. Am. Chem. Soc.* **2022**, *144*, 20834–20846.
[36] F. R. Chen, G. Coudurier, J. F. Joly, J. C. Vedrine, *J. Catal.* **1993**, *143*, 616–626.
[37] C. R. Vera, C. L. Pieck, K. Shimizu, C. A. Querini, J. M. Parera, *J. Catal.* **1999**, *187*, 39–49.
[38] J. Huang, J. Liu, L. Tian, X. Li, X. Ma, X. Yu, Q. Guo, J. Zhao, *Chem. Eng. J.* **2021**, *412*, 128621.
[39] J. M. Costantini, F. Beuneu, *Phys. Stat. Sol.* **2007**, *4*, 1258–1263.
[40] R. A. Elsalamony, D. R. Abd El-Hafiz, M. A. Ebiad, A. M. Mansour, L. S. Mohamed, *RSC Adv.* **2013**, *3*, 23791–23800.
[41] A. A. Marciniak, F. J. F. S. Henrique, A. F. F. de Lima, O. C. Alves, C. R. Moreira, L. G. Appel, C. J. A. Mota, *J. Mol. Catal.* **2020**, *493*, 111053.
[42] O. E. Everett Espino, P. C. Zonetti, R. R. Celin, L. T. Costa, O. C. Alves, J. C. Spadotto, L. G. Appel, R. R. De Avillez, *Catal. Sci. Technol.* **2022**, *12*, 1324–1338.
[43] E. Mamontov, T. Egami, R. Brezny, M. Koranne, S. Tyagi, *J. Phys. Chem. B* **2000**, *104*, 11110–11116.
[44] A. A. Marciniak, O. C. Alves, L. G. Appel, C. J. A. Mota, *J. Catal.* **2019**, *371*, 88–95.
[45] E. P. Saliba, E. L. Sesti, F. J. Scott, B. J. Albert, E. J. Choi, N. Alaniva, C. Gao, A. B. Barnes, *J. Am. Chem. Soc.* **2017**, *139*, 6310–6313.
[46] E. Morra, E. Giamello, S. Van Doorslaer, G. Antinucci, M. D'Amore, V. Busico, M. Chiesa, *Angew. Chem. Int. Ed.* **2015**, *54*, 4857–4860.
[47] Q. Zhu, Y. Peng, L. Lin, C. M. Fan, G. Q. Gao, R. X. Wang, A. W. Xu, *J. Mater. Chem. A* **2014**, *2*, 4429–4437.
[48] H. Xie, N. Li, X. Chen, J. Jiang, X. Zhao, *Appl. Surf. Sci.* **2020**, *511*, 145597.
[49] J. Wan, W. Chen, C. Jia, L. Zheng, J. Dong, X. Zheng, Y. Wang, W. Yan, C. Chen, Q. Peng, D. Wang, Y. Li, *Adv. Mater.* **2018**, *30*, 1705369.
[50] K. Yang, J. Liu, R. Si, X. Chen, W. Dai, X. Fu, *J. Catal.* **2014**, *317*, 229–239.
[51] J. Xie, M. Yao, W. Gao, Z. Su, X. Yao, *J. Alloys Compd.* **2019**, *772*, 324–331.
[52] C. Wang, G. Garbarino, L. F. Allard, F. Wilson, G. Busca, M. Flytzani-Stephanopoulos, *ACS Catal.* **2016**, *6*, 210–218.
[53] G. R. Jenness, M. A. Christiansen, S. Caratzoulas, D. G. Vlachos, R. J. Gorte, *J. Phys. Chem. C* **2014**, *118*, 12899–12907.
[54] J. F. DeWilde, H. Chiang, D. A. Hickman, C. R. Ho, A. Bhan, *ACS Catal.* **2013**, *3*, 798–807.
[55] Z. Qi, L. Chen, S. Zhang, J. Su, G. A. Somorjai, *J. Am. Chem. Soc.* **2021**, *143*, 60–64.
[56] J. Cornejo-Romero, A. Solis-Garcia, S. M. Vega-Diaz, J. C. Fierro-Gonzalez, *J. Mol. Catal.* **2017**, *433*, 391–402.
[57] S. Luo, H. Song, D. Philo, M. Oshikiri, T. Kako, J. Ye, *Appl. Catal. B* **2020**, *272*, 118965.
[58] M. Martinelli, C. D. Watson, G. Jacobs, *Int. J. Hydrogen Energy* **2020**, *45*, 18490–18501.
[59] S. Rousseau, O. Marie, P. Bazin, M. Daturi, S. Verdier, V. Harlé, *J. Am. Chem. Soc.* **2010**, *132*, 10832–10841.
[60] E. O. Gonzalez-Yañez, G. A. Fuentes, M. E. Hernández-Terán, J. C. Fierro-Gonzalez, *Appl. Catal. A* **2013**, *464–465*, 374–383.
[61] G. Jacobs, R. A. Keogh, B. H. Davis, *J. Catal.* **2007**, *245*, 326–337.
[62] M. Martinelli, J. D. Castro, N. Alhraki, M. E. Matamoros, A. J. Kropf, D. C. Cronauer, G. Jacobs, *Appl. Catal. A* **2021**, *610*, 117947.
[63] M. Martinelli, R. Garcia, C. D. Watson, D. C. Cronauer, A. J. Kropf, G. Jacobs, *Nanomaterials* **2021**, *11*, 1–24.
[64] Z. Rajabi, L. Jones, M. Martinelli, D. Qian, D. C. Cronauer, A. J. Kropf, C. D. Watson, G. Jacobs, *Catalysts* **2021**, *11*, 1104.
[65] M. Martinelli, C. D. Watson, G. Jacobs, *Int. J. Hydrogen Energy* **2020**, *45*, 18490–18501.
[66] J. Cornejo-romero, A. Solis-garcia, S. M. Vega-diaz, J. C. Fierro-gonzalez, *J. Mol. Catal.* **2017**, *433*, 391–402.
[67] M. B. Boucher, M. D. Marcinkowski, M. L. Liriano, C. J. Murphy, E. A. Lewis, A. D. Jewell, M. F. G. Mattera, G. Kyriakou, M. Flytzani-stephanopoulos, E. C. H. Sykes, *ACS Nano* **2013**, *7*, 6181–6187.
[68] C. Wang, M. Yang, M. Flytzani-stephanopoulos, *AIChE J.* **2016**, *62*, 429–439.
[69] A. P. Farkas, Á. Szitás, D. Jurdi, K. Palotás, J. Kiss, Z. Kónya, *Appl. Catal. A* **2020**, *592*, 117440.
[70] A. Gazsi, A. Koós, T. Bánsági, F. Solymosi, *Catal. Today* **2011**, *160*, 70–78.
[71] T. Nishiguchi, T. Matsumoto, H. Kanai, K. Utani, *Appl. Catal. A* **2005**, *279*, 273–277.
[72] M. Xu, M. J. L. Gines, A. Hilmen, B. L. Stephens, E. Iglesia, *J. Catal.* **1997**, *147*, 130–147.

Manuscript received: May 10, 2024
Accepted manuscript online: June 3, 2024
Version of record online: July 22, 2024